Preserving axosomatic spiking features despite diverse dendritic morphology

Etay Hay, Felix Schürmann, Henry Markram and Idan Segev

J Neurophysiol 109:2972-2981, 2013. First published 27 March 2013; doi:10.1152/jn.00048.2013

J Neurophysiol 109: 2972–2981, 2013.
First published March 27, 2013; doi:10.1152/jn.00048.2013.

Preserving axosomatic spiking features despite diverse dendritic morphology

Etay Hay,[1] Felix Schürmann,[3] Henry Markram,[3] and Idan Segev[1,2]

[1]*Interdisciplinary Center for Neural Computation and Edmond and Lily Safra Center for Brain Sciences, The Hebrew University of Jerusalem, Jerusalem, Israel;* [2]*Department of Neurobiology, The Hebrew University of Jerusalem, Jerusalem, Israel; and* [3]*Brain Mind Institute, Ecole Polytechnique Fèdèrale de Lausanne, Lausanne, Switzerland*

Submitted 22 January 2013; accepted in final form 25 March 2013

Hay E, Schürmann F, Markram H, Segev I. Preserving axosomatic spiking features despite diverse dendritic morphology. *J Neurophysiol* 109: 2972–2981, 2013. First published March 27, 2013; doi:10.1152/jn.00048.2013.—Throughout the nervous system, cells belonging to a certain electrical class (e-class)–sharing high similarity in firing response properties–may nevertheless have widely variable dendritic morphologies. To quantify the effect of this morphological variability on the firing of layer 5 thick-tufted pyramidal cells (TTCs), a detailed conductance-based model was constructed for a three-dimensional reconstructed exemplar TTC. The model exhibited spike initiation in the axon and reproduced the characteristic features of individual spikes, as well as of the firing properties at the soma, as recorded in a population of TTCs in young Wistar rats. When using these model parameters over the population of 28 three-dimensional reconstructed TTCs, both axonal and somatic ion channel densities had to be scaled linearly with the conductance load imposed on each of these compartments. Otherwise, the firing of model cells deviated, sometimes very significantly, from the experimental variability of the TTC e-class. The study provides experimentally testable predictions regarding the coregulation of axosomatic membrane ion channels density for cells with different dendritic conductance load, together with a simple and systematic method for generating reliable conductance-based models for the whole population of modeled neurons belonging to a particular e-class, with variable morphology as found experimentally.

dendrite; ion channel; model; pyramidal cell; spiking

NEURONS THAT SHARE SIMILAR firing response properties are often classified as a specific electrical class (e-class), e.g., bursting, regular firing, and adapting (Larkman and Mason 1990; Nowak et al. 2003). Within a given e-class, neurons have largely variable dendritic morphologies. Layer 5 thick-tufted pyramidal cells (TTCs) are characterized by prototypical morphological features and can also be classified as an e-class, differing even from their neighboring L5 thin-tufted pyramidal cells in spike threshold, amplitude, half-width, and initial burst interspike interval (ISI) (Le Be et al. 2007). Nevertheless, although TTCs have unique morphological characteristics, they vary widely in their dendritic length, surface area, and the complexity of their branching pattern (Le Be et al. 2007; Romand et al. 2011; Zhu 2000). A significant portion of the ionic current entering the axon via its membrane ion channels leaks axially into the soma and dendrites; similarly, currents entering the soma via its membrane ion channels leak primarily into the dendrites (Rall 1959). Differences in cell morphology are reflected in both of these conductance loads and are, therefore, expected to affect the firing features of the soma/axon "hot" region (Baranauskas et al. 2013; Mainen and Sejnowski 1996).

Previous experimental studies have shown that the uncoupling of soma from the dendrites in Purkinje cells, or from the apical dendrites in TTCs, significantly impacts various features of somatic firing (Bekkers and Hausser 2007) and synaptic integration (Bekkers 2011). Modeling studies have demonstrated the high sensitivity of neuronal firing to changes in dendritic diameter, length, or entire morphology (Hay et al. 2011; Mainen and Sejnowski 1996; Roberts et al. 2009; van Elburg and van Ooyen 2010; Weaver and Wearne 2008). Previous studies characterized the effect of dendritic morphology variability in TTCs on the coupling between dendritic and axosomatic spiking zones (Schaefer et al. 2003). Other studies explored the effect of morphology variability within hippocampal CA3 neurons on somatic bursting (Krichmar et al. 2002; Migliore et al. 1995). However, there has not been a systematic modeling study exploring how different dendritic morphologies belonging to the same morphological type affect the firing pattern of the cells in response to somatic step-current stimulation, which is used to characterize the e-class (but see De Schutter and Bower 1994 for testing a Purkinje model somatic response to step current over 3 different Purkinje cells). Indeed, if the variability in dendritic morphology (namely in the conductance load imposed by the dendrites on the axon/soma region) in a given e-class is large, a large variability in axosomatic firing is expected compared with the experimental variability. Therefore, some compensatory mechanism is necessary for retaining the characteristics of the firing properties in this e-class (Golowasch et al. 1999; Grubb et al. 2011).

We have previously shown that adult rat TTC model parameters fitted for an exemplar morphology were not guaranteed to yield proper firing when tested on other morphologies (Hay et al. 2011). In this study, we focused on TTCs of young rats and explored the effect of dendritic morphology diversity on the axosomatic spiking characteristics. At this age, these cells do not exhibit dendritic calcium spikes (Zhu 2000). We demonstrate the marked dependence of somatic firing characteristics on TTCs dendritic morphology and propose a simple experimentally testable scaling rule of ion channel density, at both axon and soma, so as to preserve the firing of TTC e-class, despite large morphological variability of their dendritic tree. Alternative possibilities for compensating for differences in dendritic load are also discussed.

Address for reprint requests and other correspondence: Corresponding author: I. Segev, Interdisciplinary Ctr. for Neural Computation, Hebrew Univ., Edmond Safra Campus, Givat Ram, Jerusalem 91904, Israel (e-mail: idan@lobster.ls.huji.ac.il).

Table 1. *Experimental values of spiking features for the thick-tufted pyramidal cell electrical class*

Feature	Low Frequency	Medium Frequency	High Frequency
1. Spike frequency, Hz	6.8 ± 1.1	14 ± 1.2	20.8 ± 1.6
2. Adaptation index	0.03 ± 0.01	0.008 ± 0.003	0.006 ± 0.002
3. ISI-CV	0.09 ± 0.13	0.06 ± 0.04	0.1 ± 0.05
4. Initial burst ISI, ms	76.5 ± 24.2	28 ± 8	8.9 ± 5
5. First spike latency, ms	27.8 ± 3.8	11.5 ± 2	6.5 ± 1
6. AP peak, mV	23.9 ± 4.2	20.3 ± 4.1	20.3 ± 3.9
7. AHP depth, mV	−62.6 ± 3	−59.1 ± 2.8	−56 ± 4.1
8. Slow AHP depth, mV	−63.4 ± 3	−59.2 ± 2.8	−56.1 ± 4.1
9. AP half-width, ms	2.0 ± 0.8	2.8 ± 0.8	3 ± 0.8

Values are means ± SD. Features are given of the response to somatic step current for three different step amplitudes yielding low, medium, and high firing frequencies (see MATERIALS AND METHODS). ISI-CV, interspike interval coefficient of variation; AP, action potential; AHP, afterhyperpolarization.

MATERIALS AND METHODS

Experimental Data

Firing response to depolarizing somatic step currents (step-current firing). We used experimental voltage traces of the firing response to step currents in young [postnatal *day 14* (P14)] Wistar rat TTCs in vitro (see Le Be et al. 2007 for methods). Briefly, cells were injected at the soma with depolarizing step current of variable amplitudes, each 2 s in duration, and recorded in whole cell configuration at 33–35°C. The data were obtained from 20 TTCs, each with 10–15 different suprathreshold step-current amplitudes. The response to each amplitude was measured twice.

Cell morphologies. We used 28 morphologies of age P14 Wistar rat TTCs stained with biocytin and three-dimensional (3D) reconstructed under light microscopy using Neurolucida (Microbrightfield). All morphologies were checked for *z*-axis noise and improper diameters and were corrected for 25% tissue shrinkage. These morphologies are also available in NeuroMorpho database (Ascoli et al. 2007), under H. Markram.

Test set. To test the generalization of our results (Szilagyi and De Schutter 2004), we used a separate set of seven reconstructed young rat TTCs, which were provided to NeuroMorpho by A. Korngreen.

Firing features. We dissected the step-current firing response of TTCs into multiple features, e.g., spike frequency, spike half-width, and adaptation index (see Hay et al. 2011, and Table 1), and extracted their statistics (mean and standard deviation per feature) from the experimental traces. The frequency-current (*f-I*) relations of the 20 experimental cells were normalized using a reference frequency, as described previously (Hay et al. 2011). In the present study, however, we used a lower reference frequency (2 Hz), since we found it more useful and accurate for comparing the *f-I* relations of different cells. We note that the value of the reference frequency did not significantly influence the firing feature statistics derived from the data. We extracted features from three different step-current amplitudes corresponding to low, medium, and high firing frequencies (see Table 1), to capture the *f-I* relation of TTCs. The average step amplitudes were computed by averaging the amplitudes across cells, yielding 350, 610, and 1,050 pA for the three current steps, and −123 pA for the average holding DC current. This current was used, in addition to the current step stimuli, to hold each cell's resting membrane potential around −80 mV, thus normalizing for the difference in resting potential between cells.

Modeling

Axon morphology. The model axon consisted of axon initial segment (AIS) of 50 μm in length (Palmer and Stuart 2006), divided into compartments of 5 μm each, with diameter tapering from 3 to 1 μm as measured experimentally (Kole et al. 2008). Beyond the AIS, we included a myelin section of length 1,000 μm (see below for electrical parameters).

Free parameters. The 17 free parameters in the optimization included the maximal conductance ($\bar{g}$) of the set of ion channels assumed to be located in the axon and soma (8 ion channels in the axon and 7 ion channels in the soma), as well as the decay time constant for the Ca^{2+} buffer in the axon and the soma (see Table 2). We assumed the existence of eight ionic conductance mechanisms in the axon: fast inactivating Na^+ current (Na_t), persistent Na^+ current (Na_p), fast inactivating K^+ current, slow inactivating K^+ current, fast non-inactivating K^+ current ($Kv_{3.1}$), small-conductance Ca^{2+}-activated K^+ current, high-voltage Ca^{2+} current, and low-voltage Ca^{2+} current. In addition, we included a Ca^{2+} buffer mechanism. We assumed that all of the above mechanisms exist in the soma as well, except for Na_p (Astman et al. 2006). The conductance mechanisms were modeled using Hodgkin-Huxley formalism, as described previously (see Hay et al. 2011 for details and kinetic equations of ion channels and calcium buffer).

Other parameters. As indicated by a previous experimental study from which our laboratory derived the Na_t channel kinetics (Colbert and Pan 2002), the half-maximum voltage ($V_{1/2}$) for activation of Na_t in the soma was more depolarized than in the axon by 13 mV; the slope of the activation curve was 9 and 7 mV^{-1} in the axon and soma, respectively; and the $V_{1/2}$ for inactivation was more depolarized in the soma than in the axon by 5 mV (Colbert and Pan 2002). We note that similar differences were also observed in other experimental studies (Hu et al. 2009; Kole et al. 2008). To reduce the required Na_t density in our models, we found it necessary to shift the $V_{1/2}$ for inactivation of Na_t by +10 mV in the axon and soma, a parameter which (unlike

Table 2. *Parameter range used in the evolutionary algorithm*

Axon			Soma		
Parameter	Lower Limit	Upper Limit	Parameter	Lower Limit	Upper Limit
$\bar{g}_{Nat}$, pS/μm^2	0	10,000	$\bar{g}_{Nat}$, pS/μm^2	0	3,000
$\bar{g}_{Nap}$, pS/μm^2	0	100	$\bar{g}_{Kp}$, pS/μm^2	0	10,000
$\bar{g}_{Kp}$, pS/μm^2	0	10,000	$\bar{g}_{Kt}$, pS/μm^2	0	1,000
$\bar{g}_{Kt}$, pS/μm^2	0	1,000	$\bar{g}_{Kv3.1}$, pS/μm^2	0	10,000
$\bar{g}_{Kv3.1}$, pS/μm^2	0	10,000	$\bar{g}_{SK}$, pS/μm^2	0	10,000
$\bar{g}_{SK}$, pS/μm^2	0	10,000	$\bar{g}_{CaHVA}$, pS/μm^2	0	100
$\bar{g}_{CaHVA}$, pS/μm^2	0	100	$\bar{g}_{CaLVA}$, pS/μm^2	0	1,000
$\bar{g}_{CaLVA}$, pS/μm^2	0	1,000	τ_{decay}, ms	20	1,000
τ_{decay}, ms	20	1,000			

$\bar{g}$, Maximal conductance; Na_t, fast inactivating Na^+ current; Na_p, persistent Na^+ current; K_t, fast inactivating K^+ current; K_p, slow inactivating K^+ current; $Kv_{3.1}$, fast non-inactivating K^+ current; SK, small-conductance Ca^{2+}-activated K^+ current; Ca_{HVA}, high-voltage Ca^{2+} current; Ca_{LVA}, low-voltage Ca^{2+} current; τ_{decay}, decay time constant. See MATERIALS AND METHODS and (Hay et al. 2011) for details.

the fast activation) is likely to be less constrained in voltage-clamp experiments due to interference of other currents that were not completely blocked.

The specific membrane capacitance was set to 1 μF/cm^2 for the soma and AIS, 0.02 μF/cm^2 for the myelinated section, and 2 μF/cm^2 for the basal and apical dendrites, to correct for dendritic spine area (Holmes and Rall 1992; Larkman 1991). The axial resistance was set to 100 Ω·cm for all compartments (Stuart and Spruston 1998). The specific membrane conductance was set to 0.4 pS/μm^2 (Mainen and Sejnowski 1996), with twice that value for the dendrites corresponding to the spine compensation for membrane capacitance. The leak reversal potential was -75 mV. In addition, we included the nonspecific cation current (I_h) in both the soma and dendrites. The distribution function of I_h was uniform in the soma and basal dendrites and exponentially increased in the apical dendrites, as previously described (Hay et al. 2011). We set the base density for the I_h current to 0.4 pS/μm^2. These parameters ensured that the models exhibited basic electrical properties that were in agreement with the experimental statistics. The membrane time constant was 20.9 ms, and the input resistance (R_{in}) was 47.3 MΩ in the models of the exemplar cell (no. 21 in Fig. 1), in agreement with the experimental estimates for the membrane time constant of 20 $\pm$ 6 ms (Le Be et al. 2007) and R_{in} of 50.6 $\pm$ 12.5 MΩ (Zhu 2000). Resting membrane potential in the exemplar models was -72.6 mV in the soma and -68.9 mV in the apical tuft, in agreement with the experimental estimates of -73.4 $\pm$ 2.4 mV and -68.5 $\pm$ 2.7 mV, respectively (Zhu 2000). The holding potential was -77.5 mV under the average holding current (-123 pA, see above), in agreement with our experimental dataset statistics (-79 $\pm$ 0.7 mV).

Optimization algorithm. Firing features and their experimental variability served as objectives for fitting detailed conductance-based models (CBMs) of the reconstructed TTC, utilizing a multiobjective indicator-based evolutionary algorithm (Beume et al. 2007; Zitzler and Kunzli 2004). This type of evolutionary algorithm converged faster (a factor of 2–4), better (a factor of 1.5–2), and more robustly than the elitist nondominated sorting evolutionary algorithm we have previously used (Hay et al. 2011). We divided the 3D reconstructed morphologies into compartments, each at most 20 μm long, resulting in an average of about 200 compartments per modeled cell. The algorithmic optimization and all simulations were conducted using NEURON (Carnevale and Hines 2006). For the evolutionary algorithm, we used a population size of 1,000 and 500 generations, running on 1024 cores of an IBM BlueGene/P supercomputer hosted by CADMOS and accessible to the Blue Brain Project (Markram 2006). Average runtime per optimization was 5 h.

Objectives. The objectives of the optimization procedure were the various features of the spiking response for the three step-current amplitudes (see above and Table 1). To reduce the number of objectives, we lumped each triplet of feature values (in the responses to three current step amplitudes) into a single objective (Hay et al. 2011). In addition, we included two additional rate objectives: one objective ensures that the model fires at the reference (2 Hz, see above) frequency in response to the average current step needed for the experimental TTCs to fire in this frequency. The second objective ensures that the *f-I* relationship is maintained also for very large current step amplitude (5 nA) beyond what we have in our reference dataset (see Stafstrom et al. 1984).

Acceptable models. From the sets of parameter combinations yielded by the evolutionary algorithm, we accepted the set of models that reproduced step-current firing features (see Table 1) to within 3 standard deviations (SD) from the experimentally measured mean per feature. We repeated the optimization process with at least three different randomization seeds to avoid single-run correlations between the parameters. We, therefore, consider the parameter ranges in our sets of models as good approximations of the complete ranges of possible values. Each of the sets of models discussed in the study comprised 500 acceptable models on average.

Calculating the conductance load. The dendrite-to-soma conductance ratio (ρ) is defined as: $\rho = g_{in,dendrite}/g_{in,soma}$, where $g_{in,soma}$ is the input conductance of the isolated soma, and $g_{in,dendrite}$ is the input conductance at the soma origin without the presence of a soma, namely, the input conductance of dendrites and axon at their soma junction point (Rall 1959). We note that, since the input conductance due to the dendrites/axon alone is $g_{in,dendrite} = g_{in} - g_{in,soma}$, where

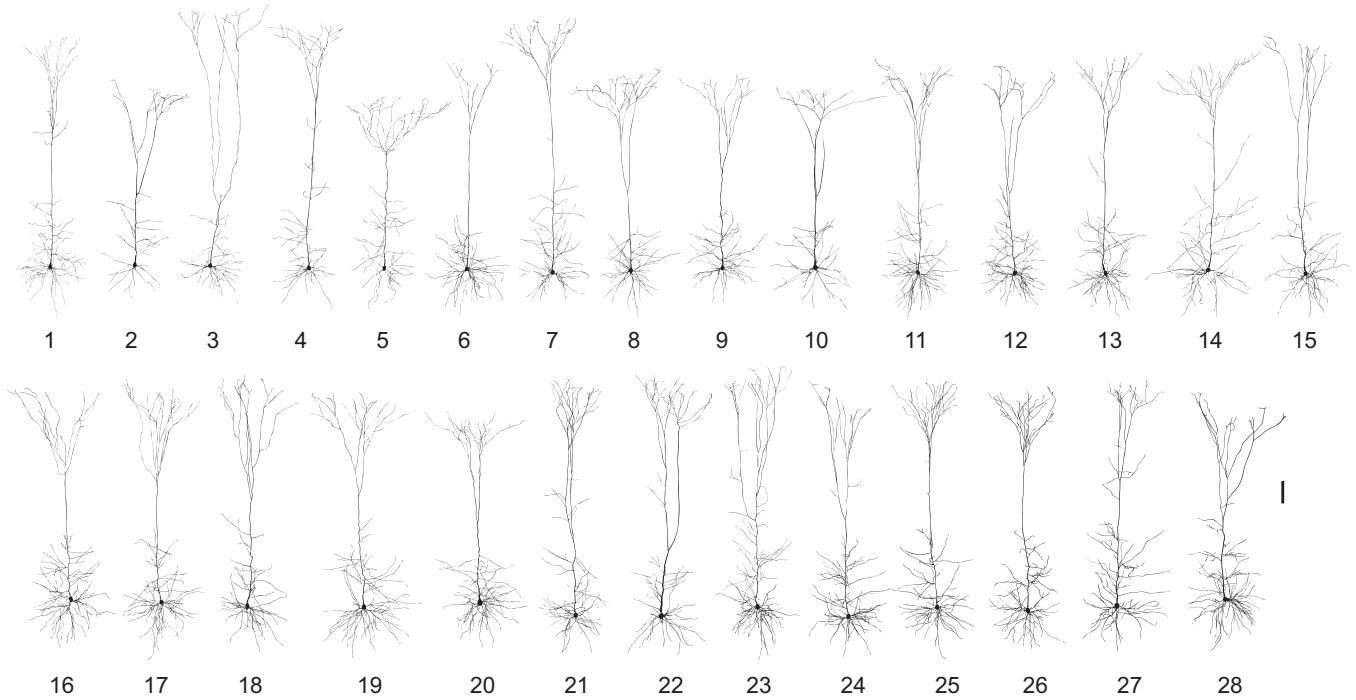

Fig. 1. Variability of dendritic morphology in L5 thick-tufted pyramidal cells (TTCs). Shown is the set of 28 L5 TTCs of young rats (age postnatal *day 14*), reconstructed in three-dimension, that were used in the present modeling study. Scale bar is 100 μm. Morphometric properties of these cells are provided in Table 3.

g_{in} is the total input conductance (soma, dendrites and axon) measured at the soma, $\rho = (g_{in} - g_{in,soma})/g_{in,soma}$.

We calculated ρ using strictly passive models by measuring the input conductance at the soma of the cell model (g_{in}), and that of the soma alone, with the axon and dendrites removed ($g_{in,soma}$). The conductance load on the AIS (ρ_{axon}) was computed similarly, by measuring the input conductance at the beginning of the AIS of the cell model (10 μm from the soma), and that of the AIS alone (with soma, dendrites, and myelin section removed).

RESULTS

The set of 28 TTC morphologies used in this study is depicted in Fig. 1, sorted by the total membrane surface area. Table 3 summarizes key morphological properties of these cells. The statistics of this dataset matched the experimental statistics reported previously (Romand et al. 2011), and thus indicated that the set of morphologies faithfully represents the TTC population in young Wistar rats. We note that the difference in surface area between morphologies was not only due to differences in total dendrite length, but also to differences in dendritic diameter. For example, the morphologies with smallest (Fig. 1, *cell 1*) and largest (Fig. 1, *cell 28*) dendritic surface area (19,230 μm^2 vs. 63,493 μm^2) differed less in their total dendrite length (12,900 μm vs. 15,178 μm) than in the average dendrite diameter (0.5 μm vs. 1.3 μm).

Deterioration of Model Performance with Varying TTC Morphology

We selected an exemplar cell (*cell 21* in Fig. 1) with R_{in} = 47.3 MΩ that was closest to the average of the TTC dataset. Due to the importance of axonal morphology for spike initiation and back-propagation into the soma (Mainen et al. 1995), we constructed a detailed morphology of the axon according to the average tapering measured in TTCs (see MATERIALS AND METHODS). We embedded a set of active conductance mechanisms in the axon and soma of the exemplar cell and optimized their densities (Table 2) to generate a set of CBMs constrained by the experimental statistics of key features of TTC firing response to somatic depolarizing step current (Table 1). In the set of models we have generated, different combinations of ion channel densities yielded similar firing feature values (Goaillard et al. 2009), as well as a variety of feature values that spanned the experimental variability for most of the target features (Gunay et al. 2008). The density of Na_t in the model axon was 6,000 pS/μm^2 on average, in agreement with recent estimates (Kole et al. 2008; Yu et al. 2008). The average ratio of axonal to somatic Na_t densities was 2.5:1, also in agreement with recent estimates (Fleidervish et al. 2010).

Feature values in our experimental dataset varied up to 3 SD from the experimental average. Since the aim of the optimization was to generate models that fire in accordance with the TTC e-class statistics rather than fit a particular TTC trace, we considered, as acceptable, TTC models that exhibited feature values within 3 SD from the average (see MATERIALS AND METHODS). Figure 2*A* shows an example for such a model (see Table 4 for parameter values of this model). In response to the three current steps (Table 1), this model generated spike frequency of 0.7 SD from the experimental mean, adaptation index 1.4 SD, ISI-coefficient of variation (CV) 0.5 SD, initial burst ISI 2.1 SD, first spike latency 1.6 SD, action potential (AP) peak 1.3 SD, afterhyperpolarization (AHP) depth 1.8 SD, slow AHP depth 1.7 SD, and spike half-width 2.2 SD from the experimental mean. In this figure, the response to the current step yielding medium firing frequency is shown (see Table 1). However, when these same model parameters were tested on the other 27 reconstructed cells (with step-current amplitudes adjusted according to their individual R_{in} values), the firing features differed among modeled cells, and for 13 cells they deviated significantly (beyond 3 SD) from the experimental mean. For example, testing the parameter set with the cell shown in Fig. 2*B* (*cell 4* in Fig. 1) resulted in deviant feature values of AP shape (e.g., AHP of 3.5 SD and AP peak of 3.1 SD from the experimental mean). When simulating the parameter set with the cell shown in Fig. 2*C* (*cell 26* in Fig. 1), the model generated a highly irregular pattern of spikes that included numerous doublets (ISI-CV was 12.6 SD). In the case of the cell shown in Fig. 2*D* (*cell 28* in Fig. 1), only a single spike could be generated, followed by a plateau potential lasting through the duration of the current step. These two firing behaviors were never found experimentally in TTCs.

These simulations demonstrate that, in the population of L5 TTCs, the variability in cell morphology has a significant impact on the firing responses of the cells to somatic current steps. The same set of axonal and somatic ion conductance densities that gives rise to appropriate firing for this e-class in a particular cell does not necessarily yield appropriate firing for other cells belonging to the same e-class (Hay et al. 2011).

Model Performance Is Correlated with the Conductance Load Imposed on the Axon and Soma

A measure for the dendritic conductance load imposed on the soma is ρ (Rall 1959). This measure can be extended to assess the combined dendritic and somatic conductance load imposed on the axon initial segment, here denoted as ρ_{axon} (see MATERIALS AND METHODS). Differences in dendritic and somatic morphology may be reflected in differences in both ρ and ρ_{axon} values.

The ranges of ρ and of ρ_{axon} values of the cells in our set were quite large (21–57 and 102–347, respectively). The exemplar cell (*cell 21*) had ρ = 34 and ρ_{axon} = 189. The ρ_{axon} and ρ values of cells were mutually correlated, although not tightly (r = 0.8). Thus cells with large conductance load on the axon tended to also have a large conductance load on the soma. For example, *cell 28* (shown in Fig. 2*D*) had ρ_{axon} of 347 and ρ value of 57, whereas *cell 4* (shown in Fig. 2*B*) had a small ρ_{axon} of 118 and ρ value of 23. This correlation stems from the primary role of the conductance load imposed by the dendrites, as can be seen in the higher correlation of ρ_{axon} and ρ values with the dendritic surface area ($r > 0.9$, not shown) than with the soma surface area ($r < 0.6$, not shown). Thus the variability in the conductance load on the axon and soma

Table 3. *Morphological properties for the 28 reconstructed L5 thick-tufted pyramidal cells shown in Fig. 1*

Property	Mean	SD
Total dendritic surface area, μm^2	37,689	11,259
Area of apical dendrites, μm^2	24,858	6,731
Area of basal dendrites, μm^2	12,830	5,430
Area of soma, μm^2	1,524	277
Average dendritic diameter, μm	0.93	0.2
Total dendrite length, μm	12,758	2,114

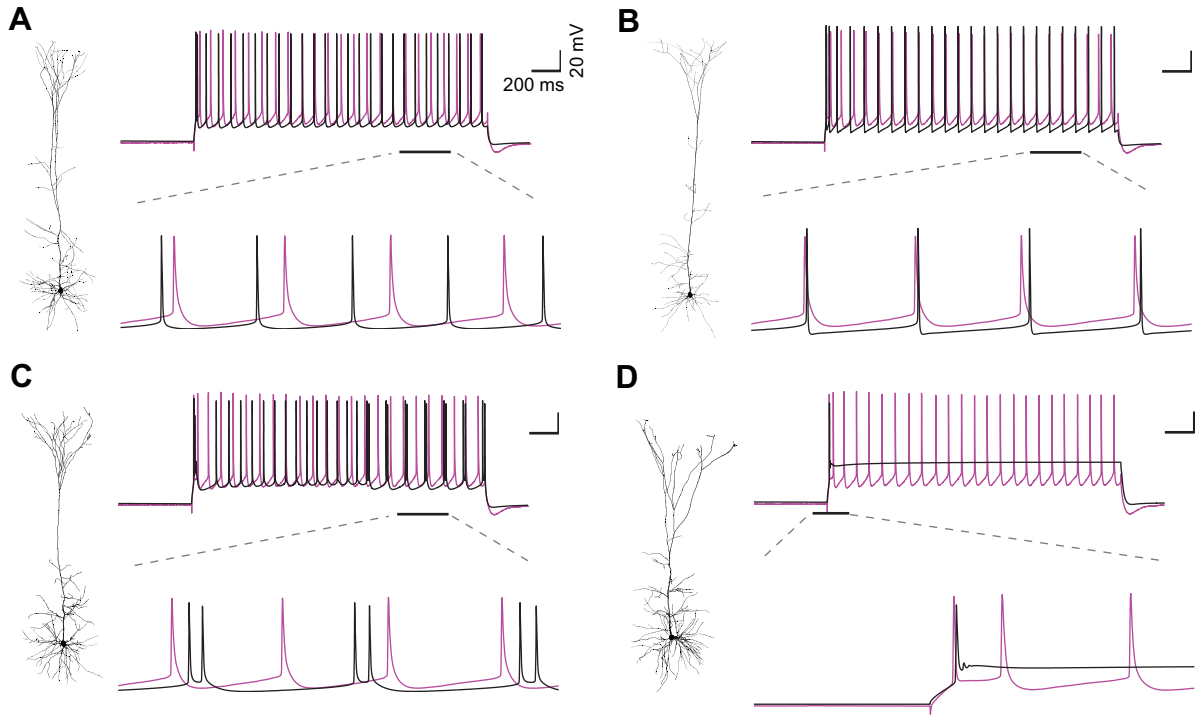

Fig. 2. Deterioration of model performance with varying cell morphology. *A*, *left*: the exemplar reconstructed neuron (*cell 21* in Fig. 1) that was used to optimize the models' response to the depolarizing step currents. *Right*: example of model responses (black traces) that were in accordance with the statistics of the experimentally observed firing (magenta) in response to 610-pA depolarizing step current injected at the soma. *B–D*: examples for using the same conductance parameters as in *A* on three other reconstructed L5 TTCs (*cell 4* in *B*, *cell 26* in *C*, and *cell 28* in *D*, as in Fig. 1) that produced large deviant responses compared with the experimental responses of the TTC electrical (e)-class. Excitable parameters for the axon and soma in the exemplar cell are given in Table 4.

stemmed primarily from dendritic variability rather than from somatic variability. Since in TTCs the axon is the site of AP initiation (Palmer and Stuart 2006), we predicted that the deviation in firing features among the modeled cells (assuming fixed channel density in the soma and axon) would be correlated with ρ_{axon}.

Indeed, most features of spike firing were sensitive to the respective ρ_{axon} value. In particular, the deviation from the mean of initial burst ISI, spike latency, AP peak, and AHP depth was strongly and linearly correlated with ρ_{axon} (Fig. 3, *D–H*, Pearson's correlation coefficient $r > 0.8$). The latency increased, initial burst ISI decreased, AP peak became more hyperpolarized, and AHP became more depolarized with increasing ρ_{axon}. By contrast, although spike frequency, adaptation index and ISI-CV were sensitive to morphology difference, they were only weakly correlated with ρ_{axon} (Fig. 3, *A–C*, $r < 0.6$). The AP half-width was correlated with ρ_{axon} ($r > 0.8$); however, the range of its change among the different modeled cells was moderate (less than 1 SD, Fig. 3*I*). Importantly, ρ_{axon} was a useful measure to clearly separate the cases with extreme deviations from the experimental firing, such as that shown in Fig. 2, *C* and *D*. These extreme deviations were observed only in models tested on cells with ρ_{axon} value considerably larger ($\rho_{axon} > 240$) than that of the exemplar cell ($\rho_{axon} = 189$). For cells with ρ_{axon} values that were smaller than that of the exemplar cell, the feature deviation due to morphological variability deteriorated more gradually with decreasing ρ_{axon}. The spike frequency deviation was better correlated with ρ ($r = 0.9$) than with ρ_{axon} ($r = 0.4$), suggesting that the conductance load imposed on the soma had a larger impact on this feature than the conductance load imposed on the axon. However, the deviations of other features were better correlated with ρ_{axon} (correlation coefficient of all features with ρ_{axon} was larger by 0.1 on average than the correlation of these features with ρ), as expected from the key role of the axon in the spike generation.

Table 4. *Parameter values used in the model for the exemplar cell (see Fig. 1, cell 21)*

Axon		Soma	
Parameter	Value	Parameter	Value
$\bar{g}_{Nat}$, pS/μm^2	6,042	$\bar{g}_{Nat}$, pS/μm^2	2,357
$\bar{g}_{Nap}$, pS/μm^2	2	$\bar{g}_{Kp}$, pS/μm^2	38
$\bar{g}_{Kp}$, pS/μm^2	2,747	$\bar{g}_{Kt}$, pS/μm^2	402
$\bar{g}_{Kt}$, pS/μm^2	832	$\bar{g}_{Kv3.1}$, pS/μm^2	1,213
$\bar{g}_{Kv3.1}$, pS/μm^2	5,326	$\bar{g}_{SK}$, pS/μm^2	1,912
$\bar{g}_{SK}$, pS/μm^2	126	$\bar{g}_{CaHVA}$, pS/μm^2	2
$\bar{g}_{CaHVA}$, pS/μm^2	14	$\bar{g}_{CaLVA}$, pS/μm^2	77
$\bar{g}_{CaLVA}$, pS/μm^2	2	τ_{decay}, ms	403
τ_{decay}, ms	21		

The parameter set was optimized for the exemplar cell, whose ρ_{axon} value is 189, and ρ value is 34.

It is important to emphasize that the deterioration of model performance was independent of which exemplar morphology was selected. For example, when the morphology with largest ρ_{axon} (*cell 28*) was selected as the exemplar for generating CBM, there was similar deterioration of latency, initial burst ISI, AHP, and AP peak with ρ_{axon} when the model parameters were tested on other cells. Hence, a fixed set of ion channel conductances when tested over cells with different dendritic

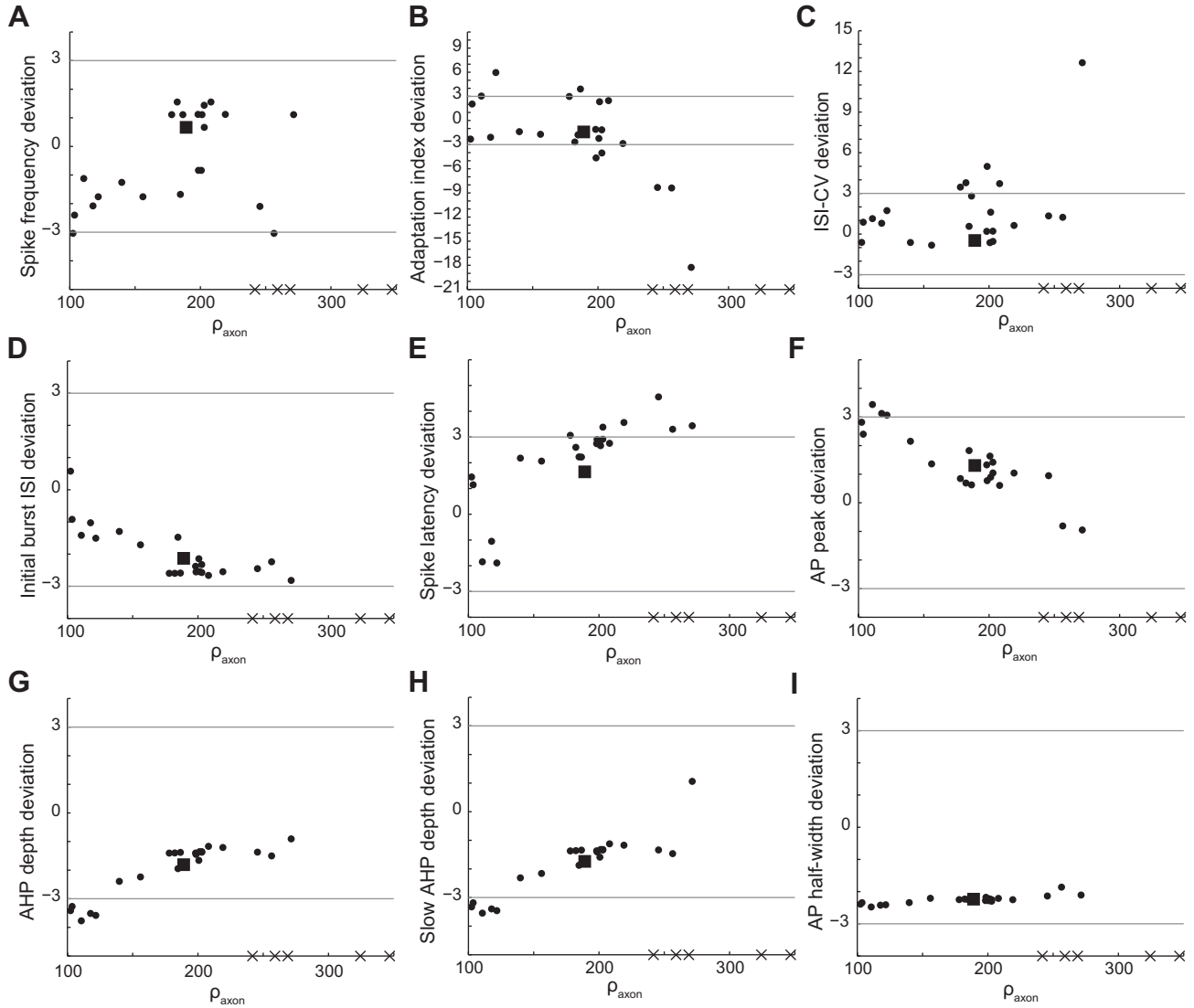

Fig. 3. Deviation of various spike/firing features for the 28 modeled cells as a function of conductance load on the axon initial segment (ρ_{axon}). *A–I*: the nine features used to characterize the firing properties of TTC e-class. Each case shows the deviation, as a function of the ρ_{axon}, from the experimental mean (in SD units), when the conductance parameters (Table 4) that were optimized for *cell 21* (large square, $\rho_{axon} = 189$) were used for all other modeled cells. Cases where one or more of the firing features could not be computed (e.g., Fig. 2*D*) are marked with an "x" on the *x*-axis. Note that such extreme failure to reproduce the firing properties of TTC e-class occurred only in models with large ρ_{axon} values. ISI, interspike interval; CV, coefficient of variation; AP, action potential; AHP, afterhyperpolarization.

morphologies could not satisfactorily replicate the experimental firing of TTC population.

We observed similar vulnerability of axosomatic firing to morphology variability also in neuron models with active dendrites constrained for back-propagating AP attenuation modeled by us previously (Hay et al. 2011). Moreover, fixing the exemplar model axon and soma parameters and searching for dendritic sodium, potassium, and calcium densities that may compensate for the dendritic load in the deviant cells did not yield acceptable models for axosomatic firing. Thus the compensation for deviant axosomatic excitability needed to be applied to the axosomatic region, irrespective of dendritic excitability (Stuart and Sakmann 1994).

To examine whether the TTC e-class exhibited similar correlations with ρ_{axon} or ρ as found in our CBMs, we used 20 of our reconstructed cells for which we also had recordings of their respective firing response. We did not find correlations between any of the firing features measured experimentally and the ρ_{axon} or ρ value of the cell ($r < 0.3$). This further supports the notion that TTCs fire as a single e-class and shows that feature values are uniformly distributed within the class, independent of their diverse dendritic morphology.

Scaling of Axonal and Somatic Ion Channels Density With ρ_{axon} and ρ Retrieves TTC e-class Model Firing

We next investigated whether we could improve model transfer across all reconstructed TTCs by simply scaling the density of the axonal and somatic ion channels according to the conductance loads ratio of the particular cell tested (ρ_{test}) and the exemplar cell ($\rho_{exemplar}$). Namely, if the density of channel i for the exemplar cell is $\bar{g}_{i,exemplar}$, then the respective $\bar{g}_i$ for the test cell is $\bar{g}_i = \bar{g}_{i,exemplar} \cdot \rho_{test}/\rho_{exemplar}$ for somatic ion channels, and $\bar{g}_i = \bar{g}_{i,exemplar} \cdot \rho_{axon,test}/\rho_{axon,exemplar}$ for axonal ion channels.

This scaling of axonal and somatic channel densities indeed served well for the entire TTC population (Fig. 4). Spike frequency, ISI-CV, initial burst ISI, AP peak voltage, AHP depth, and AP half-width were within the experimental variability for all 28 modeled TTCs (Fig. 4, *A*, *C*, *D*, *F–I*). Spike latency was mostly within the experimental variability, with only a few borderline deviations (Fig. 4*E*). The adaptation index deviations were considerably smaller than before the scaling (contrast Figs. 3*B* and 4*B*). The remaining deviations stemmed mainly from the interval between the initial burst and the third spike, after which the spike train was regular, as demonstrated by the acceptable ISI-CV values (Fig. 4*C*). Examples of model traces (Fig. 4, *J–L*) demon-

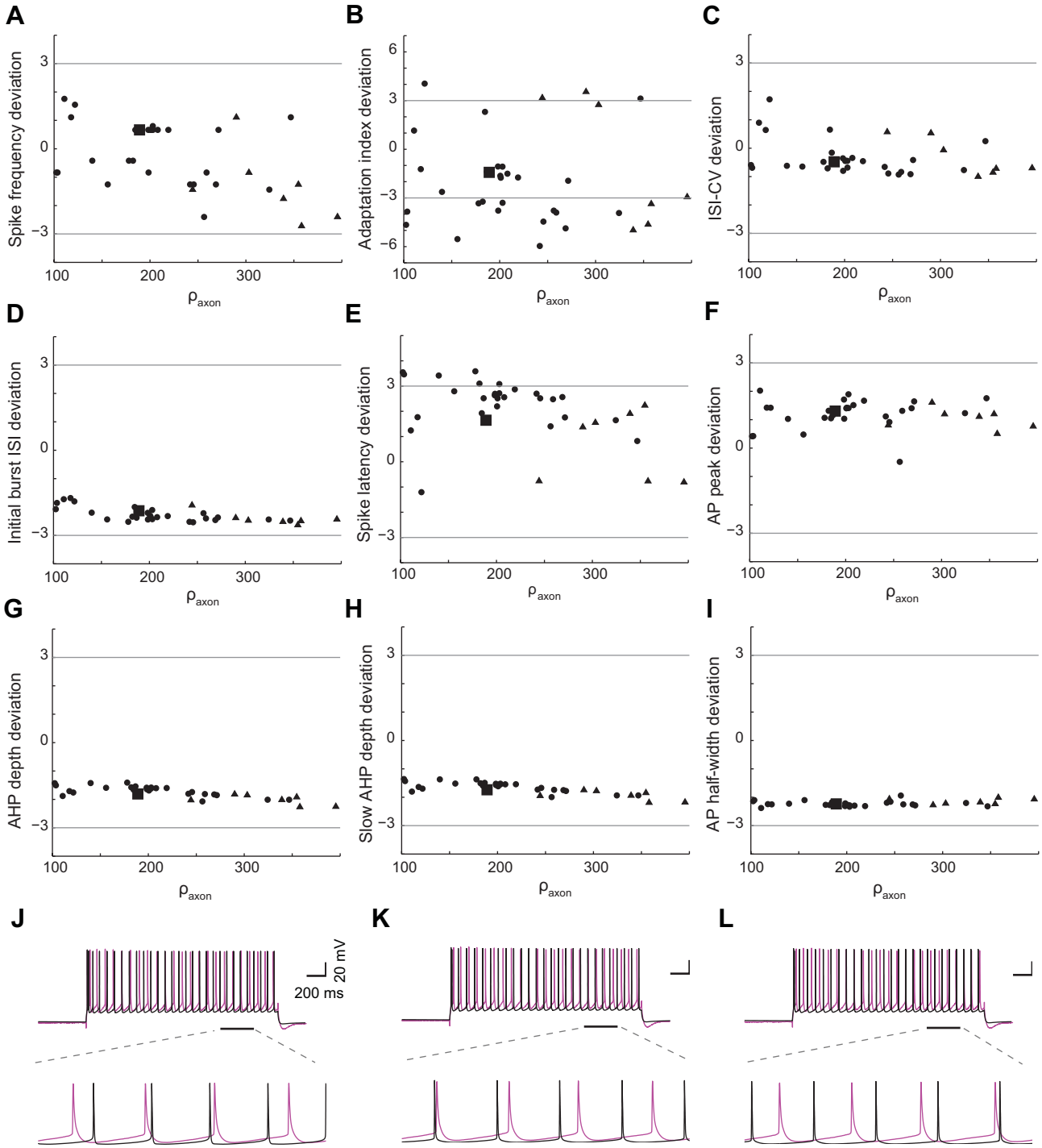

Fig. 4. Scaling axonal and somatic ion channel densities with ρ_{axon} and dendrite-to-soma conductance ratio (ρ), respectively, provided acceptable model performance over the entire TTC population. *A–I*: feature deviation across TTC population when scaling the density of all axonal ion channels with $\rho_{axon,test}/\rho_{axon,exemplar}$ and all somatic ion channels with $\rho_{test}/\rho_{exemplar}$, where ρ_{test} and $\rho_{exemplar}$ are the ρ value for tested cell and for the reference model, respectively. The conductance parameters were optimized for the exemplar cell (large square, corresponding to *cell 21* in Fig. 1). The scaled model was tested on the original set of 28 modeled cells (circles) and on an additional test set of 7 modeled cells (triangles, see MATERIALS AND METHODS). *J–L*: example traces for the three cells used in Fig. 2, *B–D* (respectively), when the parameters were scaled as described above.

strate the agreement between the step-current firing of the scaled reference model and the experimental response (compare with Fig. 2, *B–D*).

This scaling method was similarly successful when tested on the set of additional seven cells (see MATERIALS AND METHODS), further indicating that the scaling method can serve well for the entire population of TTCs. We note that the scaling procedure worked similarly well for models fitted to cells other than the exemplar (e.g., for both *cells 3* and *28*, which had small and large ρ_{axon}, respectively). Scaling only the axonal or somatic channel densities was not sufficient to satisfactorily improve the model performance. In addition, scaling both axonal and somatic channels according to either ρ_{axon} or ρ was only partially successful. Hence, the scaling had to be applied according to the particular conductance load imposed on these two different compartments.

DISCUSSION

To the best of our knowledge, this is the first study that systematically characterized and quantified the effect of dendritic morphological variability on the firing response to somatic step-current stimulation of neurons within a given e-class. We demonstrated the need to coregulate membrane conductance mechanisms to compensate for the dendritic effect on axosomatic firing. For this study, we used a central cortical neuron, the layer 5 TTCs, for which we had a large set of 3D reconstructed dendritic morphologies, as well as the firing responses to depolarizing somatic current steps. The benchmark for fitting CBMs for these cells was a set of firing features (spike height, width, rate, etc.) and their experimental variability in the TTC e-class. We showed that an acceptable CBM for any particular TTC is obtained only when the axonal and somatic ion channel densities were scaled as a function of its respective conductance load on each compartment: ρ_{axon} for the axon, and ρ for the soma. Otherwise, the firing of the modeled cells deviated from the firing characteristics of this e-class. This prediction is amenable to experimental testing, potentially by correlating the surface area of soma and proximal dendrites with the density of particular ion channels in the soma and AIS. The latter could be measured either by voltage-clamp (Kole et al. 2008; Stuart and Sakmann 1994) or by ion channel labeling (Lorincz and Nusser 2010). In addition, the study provides a simple method for generating reliable CBMs for the whole population of modeled cells with variable dendritic morphology that belong to the same e-class, without the need to repeat the optimization procedure for each neuron separately. We expect that our findings will be applicable to other neuronal cell types.

The coregulation of ion conductances for maintaining a particular firing pattern (target set point) in the face of conductance changes has been shown experimentally (Golowasch et al. 1999; Grubb et al. 2011; Kuba et al. 2010) and in theoretical studies (Ball et al. 2010). We note that compensatory mechanisms of ion channels could also be realized by a changing ion channel kinetics rather than densities (Rapp et al. 1996), as well as by any mechanism that may regulate the conductance load itself (e.g., change in axial resistance of the dendrites).

Ion Channel Densities Are Coregulated with the Dendritic Load

The impact of reduction in dendritic conductance load on AHP depth and AP peak that we found in this study was also observed in a recent modeling study (Hendrickson et al. 2011), as well as in experiments of targeted dendrotomy in Purkinje cells and layer 5 pyramidal cells (Bekkers and Hausser 2007). We successfully reproduced the latter study by uncoupling the apical dendrites in our TTC models (not shown). This further strengthens the validity of our CBMs for the TTC neuron class. We predict that dendrotomy of the basal dendrites will have a considerably larger effect on ρ and ρ_{axon} and therefore on the firing of TTCs.

The inability to fire properly in the face of an increase in dendritic load, as well as the high sensitivity of firing to perturbations of Na_t and $Kv_{3.1}$ channels, are in agreement with a recent modeling study of goldfish neurons (Weaver and Wearne 2008). This sensitivity is expected from the fine balance between fast inward and outward currents underlying the generation of APs during a prolonged step current. Importantly, such sensitivity was not observed in our model when a single spike was initiated in response to brief (several ms) suprathreshold current pulses (not shown). Thus the impact of ρ_{axon} and ρ (which are steady-state measures) became apparent only when the features of a train of APs were examined.

Model Caveats and Future Perspectives

In this study, we estimated a threefold range of ρ values in the TTC population and characterized the resulting effect on the cells' firing features. Although estimating ρ experimentally is not trivial, previous attempts to do so for cat spinal α-motoneurons suggest a twofold range of ρ values for these cells, between 5 and 10 (Nelson and Lux 1970).

One possible source of error in our estimation for ρ values might be due to the reliability of dendritic diameter measurements and possible human bias due to different reconstructors of our dataset. However, there are several indications for the small bias due to human error. *1*) The ranges of average dendritic diameter and ρ values observed in the cells of the test set from a different laboratory (see MATERIALS AND METHODS) were similar to the ranges found in our set. *2*) Our cells were reconstructed by three persons, and an analysis of the variability in reconstructed diameters between and within reconstructors did not reveal any clear bias. *3*) Although none of the 28 cells was reconstructed more than once, in our database there was another cell type (L6 basket cell) that was reconstructed independently by two persons. In this case, the reconstructions had the same average dendritic diameter and a difference of only 0.5% in the total dendritic length.

Still, to further explore the possible effect of reconstruction bias, we note that the resolution of the optical imaging device was 0.1 μm, corresponding to 0.5 SD of the average dendritic diameter (see Table 3). It therefore cannot account for more than 25% of the variability in the average diameter between the cells. Importantly, it accounts for an even smaller percentage of the variability in ρ, since the dendritic conductance load on the soma/axon region is primarily influenced by the proximal parts of the dendrites, which are thicker than the average, and are thus more reliably reconstructed. To further examine the possible effect on ρ estimates of error in dendritic diameter

measurements, we reduced the measured dendritic diameters of the cell with largest ρ by 0.1 μm and increased dendritic diameters of the cell with the smallest ρ by 0.1 μm. This reduced the range of ρ values from 2.7-fold to 1.9-fold. Hence, in the worst (and extreme) case, the optical resolution error is expected to yield a 30% error in our estimation for the variability of ρ values in the cell's population, and an error of 15–20% in the estimated ρ for individual cells.

Any noise in the 3D reconstructed soma size, as expected from incomplete optical information, may impact the estimated value of ρ. However, we verified that the input conductance of the reconstructed modeled dendrites, lacking a soma, varied 3.6-fold. Also, since the estimation of soma input conductance (which depends on its estimated area) is not likely to be biased systematically, our estimated range of ρ values seems valid. In addition, we explored the possibility that the soma size is underestimated by a factor of two for all morphologies and refitted the models accordingly. This did not change our findings significantly (not shown). Therefore, whereas the real values of ρ may be somewhat different than in our estimation, the range of ρ values that we estimated, which is the more important factor underlying our findings, is robust and stemmed primarily from dendritic rather than somatic variability.

We also examined an alternate possibility, in which the dendritic membrane leak conductance was nonuniformly increasing as in Stuart and Spruston (1998). Even though this reduced the average ρ in our population of 28 TTCs by a factor of 1.5, the range of ρ values remained threefold, and thus the vulnerability of the model performance remained.

Increasing the channel densities in the AIS serves to increase the total AIS current. Another way to increase the total AIS current is by increasing its membrane surface area while leaving the densities unchanged. However, modifying the axonal dimensions could also change the coupling between the soma and axon, as well as the passive properties of the axon. We verified that a uniform scaling of axonal diameter according to ρ_{axon} did not compensate successfully for the change in conductance load. Previous studies of electron-microscopic reconstructions suggest some correlation between axonal diameter and cell size (Sloper and Powell 1979). Future experiments should investigate whether indeed some of the compensation for changes in the conductance load is achieved by changes in the axonal morphology.

The AP half-width feature had marginal values (2–3 SD from the mean) in our models; indeed it was typically narrower in the model than in the experiments. This feature is highly influenced by the kinetics of the fast currents (Na_t and $Kv_{3.1}$), which we derived from the experimental literature. We expect that additional types of K^+ channels, as well as more accurate models of their kinetics, will improve the fit of spike width in TTC models. Furthermore, since we showed that the dendritic load (partially influenced by the presence of dendritic spines) has a significant effect on the shape of somatic spike, it is also likely that our spine-compensation factor is inaccurate (namely the dendritic resistivity and capacitance). This could be refined in the model and, together with improving channel kinetics, will yield models that span the fuller range of values for this feature, as seen experimentally.

Our choice of modeling young pyramidal cells was advantageous for isolating the effect of passive dendritic properties on axosomatic firing, since their dendrites have limited excitability (Zhu 2000). We expect similar findings in mature TTCs, since their dendritic active channels do not significantly influence their axosomatic response to step current (Hay et al. 2011; Larkum and Zhu 2002; Larkum et al. 2001; Stuart and Sakmann 1994). Still, our method could be expanded to explore the morphological effect on active dendritic properties (Torben-Nielsen and Stiefel 2010; Vetter et al. 2001), as well as on the interplay ("ping pong") between dendritic and axosomatic firing (Hay et al. 2011; Larkum et al. 1999; Schaefer et al. 2003). The method and insights we provide will also be useful in producing models with reduced morphologies (Bahl et al. 2012).

Finally, realistic cortical and other neuronal networks are composed of neurons with different morphologies belonging to the same e-class. By providing a scaling method for preserving the firing pattern of a given e-class, despite its large morphological variability, our approach enables the modeling of realistic neuronal networks with variable dendritic morphologies. The morphological variability was shown to have important implications for the robust functioning of the modeled network (Ramaswamy et al. 2012).

The model and relevant code are available in ModelDB (Hines et al. 2004).

ACKNOWLEDGMENTS

We thank Albert Gidon for useful comments, and Niklas Schmücker for contribution to the optimization algorithm.

GRANTS

This study was funded by the Israeli Science Foundation, the EPFL project fund for the Blue Brain Project, an internal fellowship to E. Hay from the Interdisciplinary Center for Neural Computation, and by the Gatsby Charitable Fund. The financial support for CADMOS and the Blue Gene/P system was provided by the Canton of Geneva, Canton of Vaud, Hans Wilsdorf Foundation, Louis-Jeantet Foundation, University of Geneva, University of Lausanne, and Ecole Polytechnique Fédérale de Lausanne.

DISCLOSURES

No conflicts of interest, financial or otherwise, are declared by the author(s).

AUTHOR CONTRIBUTIONS

Author contributions: E.H. and I.S. conception and design of research; E.H. performed experiments; E.H. analyzed data; E.H. and I.S. interpreted results of experiments; E.H. prepared figures; E.H. drafted manuscript; E.H., F.S., H.M., and I.S. edited and revised manuscript; E.H., F.S., H.M., and I.S. approved final version of manuscript.

REFERENCES

Ascoli GA, Donohue DE, Halavi M. NeuroMorpho.org: a central resource for neuronal morphologies. *J Neurosci* 27: 9247–9251, 2007.

Astman N, Gutnick MJ, Fleidervish IA. Persistent sodium current in layer 5 neocortical neurons is primarily generated in the proximal axon. *J Neurosci* 26: 3465–3473, 2006.

Bahl A, Stemmler MB, Herz AV, Roth A. Automated optimization of a reduced layer 5 pyramidal cell model based on experimental data. *J Neurosci Methods* 210: 22–34, 2012.

Ball JM, Franklin CC, Tobin AE, Schulz DJ, Nair SS. Coregulation of ion channel conductances preserves output in a computational model of a crustacean cardiac motor neuron. *J Neurosci* 30: 8637–8649, 2010.

Baranauskas G, David Y, Fleidervish IA. Spatial mismatch between the Na^+ flux and spike initiation in axon initial segment. *Proc Natl Acad Sci U S A* 110: 4051–4056, 2013.

Bekkers JM. Changes in dendritic axial resistance alter synaptic integration in cerebellar Purkinje cells. *Biophys J* 100: 1198–1206, 2011.

Bekkers JM, Hausser M. Targeted dendrotomy reveals active and passive contributions of the dendritic tree to synaptic integration and neuronal output. *Proc Natl Acad Sci U S A* 104: 11447–11452, 2007.

Beume N, Naujoks B, Emmerich M. SMS-EMOA: Multiobjective selection based on dominated hypervolume. *Eur J Oper Res* 181: 1653–1669, 2007.

Carnevale NT, Hines ML. *The NEURON Book*. Cambridge, UK: Cambridge University Press, 2006, p. xix, 457.

Colbert CM, Pan E. Ion channel properties underlying axonal action potential initiation in pyramidal neurons. *Nat Neurosci* 5: 533–538, 2002.

De Schutter E, Bower JM. An active membrane model of the cerebellar Purkinje cell. I. Simulation of current clamps in slice. *J Neurophysiol* 71: 375–400, 1994.

Fleidervish IA, Lasser-Ross N, Gutnick MJ, Ross WN. Na^+ imaging reveals little difference in action potential-evoked Na^+ influx between axon and soma. *Nat Neurosci* 13: 852–860, 2010.

Goaillard JM, Taylor AL, Schulz DJ, Marder E. Functional consequences of animal-to-animal variation in circuit parameters. *Nat Neurosci* 12: 1424–1430, 2009.

Golowasch J, Casey M, Abbott LF, Marder E. Network stability from activity-dependent regulation of neuronal conductances. *Neural Comput* 11: 1079–1096, 1999.

Grubb MS, Shu Y, Kuba H, Rasband MN, Wimmer VC, Bender KJ. Short- and long-term plasticity at the axon initial segment. *J Neurosci* 31: 16049–16055, 2011.

Gunay C, Edgerton JR, Jaeger D. Channel density distributions explain spiking variability in the globus pallidus: a combined physiology and computer simulation database approach. *J Neurosci* 28: 7476–7491, 2008.

Hay E, Hill S, Schurmann F, Markram H, Segev I. Models of neocortical layer 5b pyramidal cells capturing a wide range of dendritic and perisomatic active properties. *PLoS Comput Biol* 7: e1002107, 2011.

Hendrickson EB, Edgerton JR, Jaeger D. The capabilities and limitations of conductance-based compartmental neuron models with reduced branched or unbranched morphologies and active dendrites. *J Comput Neurosci* 30: 301–321, 2011.

Hines ML, Morse T, Migliore M, Carnevale NT, Shepherd GM. ModelDB: a database to support computational neuroscience. *J Comput Neurosci* 17: 7–11, 2004.

Holmes WR, Rall W. Estimating the electrotonic structure of neurons with compartmental models. *J Neurophysiol* 68: 1438–1452, 1992.

Hu W, Tian C, Li T, Yang M, Hou H, Shu Y. Distinct contributions of Na(v)1.6 and Na(v)12 in action potential initiation and backpropagation. *Nat Neurosci* 12: 996–1002, 2009.

Kole MH, Ilschner SU, Kampa BM, Williams SR, Ruben PC, Stuart GJ. Action potential generation requires a high sodium channel density in the axon initial segment. *Nat Neurosci* 11: 178–186, 2008.

Krichmar JL, Nasuto SJ, Scorcioni R, Washington SD, Ascoli GA. Effects of dendritic morphology on CA3 pyramidal cell electrophysiology: a simulation study. *Brain Res* 941: 11–28, 2002.

Kuba H, Oichi Y, Ohmori H. Presynaptic activity regulates Na(+) channel distribution at the axon initial segment. *Nature* 465: 1075–1078, 2010.

Larkman A, Mason A. Correlations between morphology and electrophysiology of pyramidal neurons in slices of rat visual cortex. I. Establishment of cell classes. *J Neurosci* 10: 1407–1414, 1990.

Larkman AU. Dendritic morphology of pyramidal neurones of the visual cortex of the rat. III. Spine distributions. *J Comp Neurol* 306: 332–343, 1991.

Larkum ME, Zhu JJ. Signaling of layer 1 and whisker-evoked Ca^{2+} and Na^+ action potentials in distal and terminal dendrites of rat neocortical pyramidal neurons in vitro and in vivo. *J Neurosci* 22: 6991–7005, 2002.

Larkum ME, Zhu JJ, Sakmann B. Dendritic mechanisms underlying the coupling of the dendritic with the axonal action potential initiation zone of adult rat layer 5 pyramidal neurons. *J Physiol* 533: 447–466, 2001.

Larkum ME, Zhu JJ, Sakmann B. A new cellular mechanism for coupling inputs arriving at different cortical layers. *Nature* 398: 338–341, 1999.

Le Be JV, Silberberg G, Wang Y, Markram H. Morphological, electrophysiological, and synaptic properties of corticocallosal pyramidal cells in the neonatal rat neocortex. *Cereb Cortex* 17: 2204–2213, 2007.

Lorincz A, Nusser Z. Molecular identity of dendritic voltage-gated sodium channels. *Science* 328: 906–909, 2010.

Mainen ZF, Joerges J, Huguenard JR, Sejnowski TJ. A model of spike initiation in neocortical pyramidal neurons. *Neuron* 15: 1427–1439, 1995.

Mainen ZF, Sejnowski TJ. Influence of dendritic structure on firing pattern in model neocortical neurons. *Nature* 382: 363–366, 1996.

Markram H. The blue brain project. *Nat Rev Neurosci* 7: 153–160, 2006.

Migliore M, Cook EP, Jaffe DB, Turner DA, Johnston D. Computer simulations of morphologically reconstructed CA3 hippocampal neurons. *J Neurophysiol* 73: 1157–1168, 1995.

Nelson PG, Lux HD. Some electrical measurements of motoneuron parameters. *Biophys J* 10: 55–73, 1970.

Nowak LG, Azouz R, Sanchez-Vives MV, Gray CM, McCormick DA. Electrophysiological classes of cat primary visual cortical neurons in vivo as revealed by quantitative analyses. *J Neurophysiol* 89: 1541–1566, 2003.

Palmer LM, Stuart GJ. Site of action potential initiation in layer 5 pyramidal neurons. *J Neurosci* 26: 1854–1863, 2006.

Rall W. Branching dendritic trees and motoneuron membrane resistivity. *Exp Neurol* 1: 491–527, 1959.

Ramaswamy S, Hill SL, King JG, Schurmann F, Wang Y, Markram H. Intrinsic morphological diversity of thick-tufted layer 5 pyramidal neurons ensures robust and invariant properties of in silico synaptic connections. *J Physiol* 590: 737–752, 2012.

Rapp M, Yarom Y, Segev I. Modeling back propagating action potential in weakly excitable dendrites of neocortical pyramidal cells. *Proc Natl Acad Sci U S A* 93: 11985–11990, 1996.

Roberts CB, O'Boyle MP, Suter KJ. Dendrites determine the contribution of after depolarization potentials (ADPs) to generation of repetitive action potentials in hypothalamic gonadotropin releasing-hormone (GnRH) neurons. *J Comput Neurosci* 26: 39–53, 2009.

Romand S, Wang Y, Toledo-Rodriguez M, Markram H. Morphological development of thick-tufted layer v pyramidal cells in the rat somatosensory cortex. *Front Neuroanat* 5: 5, 2011.

Schaefer AT, Larkum ME, Sakmann B, Roth A. Coincidence detection in pyramidal neurons is tuned by their dendritic branching pattern. *J Neurophysiol* 89: 3143–3154, 2003.

Sloper JJ, Powell TP. A study of the axon initial segment and proximal axon of neurons in the primate motor and somatic sensory cortices. *Philos Trans R Soc Lond B Biol Sci* 285: 173–197, 1979.

Stafstrom CE, Schwindt PC, Crill WE. Repetitive firing in layer V neurons from cat neocortex in vitro. *J Neurophysiol* 52: 264–277, 1984.

Stuart G, Spruston N. Determinants of voltage attenuation in neocortical pyramidal neuron dendrites. *J Neurosci* 18: 3501–3510, 1998.

Stuart GJ, Sakmann B. Active propagation of somatic action potentials into neocortical pyramidal cell dendrites. *Nature* 367: 69–72, 1994.

Szilagyi T, De Schutter E. Effects of variability in anatomical reconstruction techniques on models of synaptic integration by dendrites: a comparison of three Internet archives. *Eur J Neurosci* 19: 1257–1266, 2004.

Torben-Nielsen B, Stiefel KM. An inverse approach for elucidating dendritic function. *Front Comput Neurosci* 4: 128, 2010.

van Elburg RA, van Ooyen A. Impact of dendritic size and dendritic topology on burst firing in pyramidal cells. *PLoS Comput Biol* 6: e1000781, 2010.

Vetter P, Roth A, Hausser M. Propagation of action potentials in dendrites depends on dendritic morphology. *J Neurophysiol* 85: 926–937, 2001.

Weaver CM, Wearne SL. Neuronal firing sensitivity to morphologic and active membrane parameters. *PLoS Comput Biol* 4: e11, 2008.

Yu Y, Shu Y, McCormick DA. Cortical action potential backpropagation explains spike threshold variability and rapid-onset kinetics. *J Neurosci* 28: 7260–7272, 2008.

Zhu JJ. Maturation of layer 5 neocortical pyramidal neurons: amplifying salient layer 1 and layer 4 inputs by Ca^{2+} action potentials in adult rat tuft dendrites. *J Physiol* 526: 571–587, 2000.

Zitzler E, Kunzli S. Indicator-based selection in multiobjective search. *Parallel Problem Solving from Nature-PPSN VIII* 3242: 832–842, 2004.